

1 **Observed Seasonal Evolution of the Antarctic Slope**
2 **Current System off the Coast of Dronning Maud Land,**
3 **East Antarctica**

4 **Julius Lauber^{1,2}, Laura de Steur¹, Tore Hattermann¹, Elin Darelus^{2,3}**

5 ¹Norwegian Polar Institute, Tromsø, Norway

6 ²Geophysical Institute, University of Bergen, Bergen, Norway

7 ³Bjerknes Centre for Climate Research, Bergen, Norway

8 **Key Points:**

- 9 • The seasonal maximum in thermocline depth and minimum in subsurface salin-
- 10 ity occurs up to six months later over 2200 m than 1100 m isobath
- 11 • Buoyancy fluxes from sea ice melt play an important role in seasonal variations
- 12 in the baroclinic slope current strength
- 13 • Flow into the Fimbulisen cavity is strongest in spring/summer when the Antarc-
- 14 tic Slope Current is weakest

Corresponding author: Julius Lauber, julius.lauber@npolar.no

Abstract

The access of heat to the Antarctic ice shelf cavities is regulated by the Antarctic Slope Front, separating relatively warm offshore water masses from cold water masses on the continental slope and inside the cavity. Previous observational studies along the East Antarctic continental slope have identified the drivers and variability of the front and the associated current, but a complete description of their seasonal cycle is currently lacking. In this study, we utilize two years (2019-2020) of observations from two oceanographic moorings east of the prime meridian to further detail the slope front and current seasonality. In combination with climatological hydrography and satellite-derived surface velocity, we identify processes that explain the hydrographic variability observed at the moorings. These processes include (i) an offshore spreading of seasonally formed Antarctic Surface Water, resulting in a lag in salinity and thermocline depth seasonality toward deeper isobaths, and (ii) the crucial role of buoyancy fluxes from sea ice melt and formation for the baroclinic seasonal cycle. Finally, data from two sub-ice-shelf moorings below Fimbulisen show that flow at the main sill into the cavity seasonally coincides with a weaker slope current in spring/summer. The flow is directed out of the cavity in autumn/winter when the slope current is strongest. The refined description of the variability of the slope current and front contributes to a more complete understanding of processes important for ice-shelf-ocean interactions in East Antarctica.

Plain Language Summary

Ice shelves are the floating extensions of a land ice sheet. Along most of the East Antarctic coast, the water temperature below the ice shelves is close to the freezing point (-2°C). This limits the melting of the ice from below. In front of the ice shelves, relatively warm water (1°C) is located, but it usually cannot reach the ice due to a strong alongshore current, the Antarctic Slope Current. Here, we use temperature, salinity, and velocity observations from moored instruments at two locations within this current to investigate how it changes throughout the year. Our analyses are supported by two other data sets. We observe that changes in temperature, salinity, and velocity during the year happen earlier at the coast than offshore. In addition, we find that yearly sea ice melt during austral summer contributes to speeding up the Antarctic Slope Current in autumn. When the current is weakest, we observe a southward flow close to the seafloor toward Fimbulisen Ice Shelf, and a northward flow away from the shelf when the slope

47 current is strongest. A better understanding of the Antarctic Slope Current is impor-
48 tant to predict ice shelf melting in the future.

49 **1 Introduction**

50 The Antarctic Slope Front (ASF) is a key feature regulating offshore-onshore ex-
51 changes along most of the Antarctic coast (Jacobs, 1991; Thompson et al., 2018). East-
52 erly alongshore winds drive onshore Ekman transport that accumulates surface water
53 at the coast; due to continuity, this water is downwelled (Sverdrup, 1954; Mathiot et al.,
54 2011), creating the ASF. The resulting meridional sea surface height (SSH) and density
55 gradients balance a geostrophic current, the Antarctic Slope Current (ASC). The strength
56 of the ASF/ASC controls the extent to which offshore Circumpolar Deep Water, capa-
57 ble of increasing basal melting, can access the continental shelf and the ice shelf cavi-
58 ties (Smedsrud et al., 2006; Nøst et al., 2011; Nakayama et al., 2021).

59 In the Weddell Sea, the large-scale circulation is dominated by the clockwise Wed-
60 dell Gyre (Deacon, 1979; Vernet et al., 2019; Neme et al., 2021), driven by the large-scale
61 wind stress curl (Gordon et al., 1981; Armitage et al., 2018; Auger, Sallée, et al., 2022)
62 modulated by sea ice (Naveira Garabato et al., 2019). The southern limb of the gyre rep-
63 represents the ASC which in Dronning Maud Land (DML, 20°W-45°E) flows along the nar-
64 row continental shelf in close proximity to the ice shelves (Smedsrud et al., 2006; Nøst
65 et al., 2011). In this region, the meridional SSH and density gradients lead to a west-
66 ward ASC (Thompson et al., 2018) that decreases with depth (Huneke et al., 2022; Le Pailh
67 et al., 2020). In summer, a counter-current near the bottom has been observed (Heywood
68 et al., 1998; Núñez-Riboni & Fahrbach, 2009; Chavanne et al., 2010). Warm Deep Wa-
69 ter (WDW), a derivative of Circumpolar Deep Water in the Weddell Sea, is located close
70 to the coast, but suppressed below the shelf break depth due to a steep ASF (Heywood
71 et al., 1998; Hattermann, 2018; Thompson et al., 2018). This regime has been labeled
72 as the Fresh Shelf regime by Thompson et al. (2018). Despite the steep ASF, modified
73 WDW (mWDW) may cross the continental slope toward the ice shelf cavities via baro-
74 clinic eddies (Nøst et al., 2011; Hattermann et al., 2012; Thompson et al., 2014). As op-
75 posed to the West Antarctic ice shelves, however, no continuous warm water presence
76 has yet been observed in the DML ice shelf cavities (Hattermann et al., 2012; Lauber,
77 Hattermann, et al., 2023).

78 Previous analyses of the ASF/ASC system have revealed both the hydrography (Hattermann,
79 2018; Pauthenet et al., 2021) and the currents (Le Paih et al., 2020) to evolve coherently
80 along the southern rim of the Weddell Sea, following isobaths due to the conservation
81 of potential vorticity (Thompson et al., 2018). Auger, Sallée, et al. (2022) proposed that
82 the SSH is seasonally forced by the zonal ocean stress (wind stress modulated by sea ice)
83 over shallow isobaths (< 1000 m) and by ocean stress curl over deep isobaths (> 1000 m).
84 The strongest depth-mean currents from moored instruments at the prime meridian have
85 been observed in April/May over 2000 m depth, and in June over 3500 m depth, i.e. de-
86 layed by one to two months (Núñez-Riboni & Fahrback, 2009; Le Paih et al., 2020). A
87 similar delay in ASC seasonality between shallow and deep isobaths was found in circum-
88 Antarctic satellite-derived geostrophic surface velocities (Auger, Sallée, et al., 2022). This
89 feature has been hypothesized to originate from the sea ice edge seasonally moving off-
90 shore and associated changes in atmosphere-ocean momentum transfer (Núñez-Riboni
91 & Fahrback, 2009; Auger, Sallée, et al., 2022).

92 The baroclinic variability of the ASC on seasonal timescales in the Weddell Sea is
93 associated with a steepening of the ASF from March to July and a relaxing from Au-
94 gust to February (Pauthenet et al., 2021), caused by buoyancy forcing (Heywood et al.,
95 1998) and wind (Graham et al., 2013): sea ice melt and surface warming from October/November
96 on create a fresh and warm, and thus buoyant, water mass called Antarctic Surface Wa-
97 ter (ASW). It accumulates at the coast via wind-driven onshore Ekman transport, sea-
98 sonally forming a secondary, relatively shallow (< 250 m) front near the surface around
99 February to April (Heywood et al., 1998; Hattermann, 2018). It is, however, unclear to
100 what extent the seasonal production of ASW, which is accumulated at the coast, drives
101 the ASC, independently of a seasonal ocean stress increase. Eddy overturning counter-
102 acts the steepening of the ASF and secondary front (Nøst et al., 2011; Zhou et al., 2014;
103 Stewart & Thompson, 2015) and eddy-resolving models indicate that this is associated
104 with an offshore spreading of ASW (Si et al., 2023). Following the sea ice minimum, which
105 typically occurs in March, the ASW is gradually transformed into more saline Winter
106 Water (WW) via brine release due to sea ice formation (Nøst et al., 2011). Overall, our
107 knowledge of the ASF/ASC is based on a limited amount of observations and idealized
108 models and hence it is incomplete. As a consequence, it is unknown how the ASF/ASC
109 seasonality relates to warm inflow under the ice shelves along the eastern Weddell Sea.

110 In this study, we present new time series of temperature, salinity, oxygen, and ve-
 111 locity from April 2019 to December 2020, obtained from two oceanographic moorings
 112 located over isobaths of 1100 m and 2200 m east of the prime meridian. These data are
 113 introduced in section 2, along with a CTD section at 6°E, climatological hydrography
 114 (Hattermann, 2018), satellite-derived surface geostrophic velocities (Auger, Prandi, &
 115 Sallée, 2022), and mooring observations from the ice shelf cavity of Fimbulisen (located
 116 200 km downstream). Methods to analyze these data are described in section 3. The new
 117 ASF/ASC observations are presented in section 4.1, and seasonal drivers of ASF/ASC
 118 seasonality are refined using the mentioned auxiliary data sets in section 4.2. In section
 119 4.3, we assess how the seasonal ASF/ASC variability relates to the inflow into the ice
 120 shelf cavity of Fimbulisen. Finally, the results are discussed in light of the existing lit-
 121 erature in section 5, and final conclusions are given in section 6.

122 2 Data

123 Two oceanographic moorings were deployed from R/V Kronprins Haakon in March
 124 2019 during the Southern Ocean Ecosystem cruise off the DML coast and recovered from
 125 M/V Malik Arctica in December 2020 and January 2021 during the Troll Transect cruise.
 126 One mooring (DML_{deep}) was located at 6.0°E, 69.1°S over a water depth of 2166 m. The
 127 other mooring (DML_{shallow}) was located at 10.6°E, 69.4°S over a water depth of 1059 m,
 128 on the eastern flank of "Astrid Ridge" (Fig. 1a). Both moorings were equipped with one
 129 Teledyne 300 kHz ADCP and one Teledyne 150 kHz ADCP, two Nortek Aquadopp cur-
 130 rent meters, three/four Sea-Bird SBE37 MicroCATs, and 11/10 Sea-Bird SBE56 ther-
 131 mistors (DML_{deep}/DML_{shallow}). Details about the instrumentation are given in Table
 132 S1 and S2 in Supporting Information S1.

133 The mooring data are complemented by a CTD section that was taken between 70°S
 134 and 68°S along 6°E during the Troll Transect cruise in December 2020 and January 2021
 135 using an SBE 911plus CTD.

136 A climatology of temperature and salinity sections with monthly resolution obtained
 137 from instrumented seals and ship sections around 17°W between 1977 and 2016 was used
 138 (Hattermann, 2018, referred to as H18 hereafter) to support and extend the analyses from
 139 our mooring observations.

140 We also include a data set of satellite-derived SSH and surface geostrophic current
 141 anomalies (Auger, Prandi, & Sallée, 2022, referred to as A22 hereafter), spanning the

142 period from April 2013 to July 2019. These data overlap only partly with the open-ocean
143 mooring period starting in late March 2019, and instead of comparing the time series
144 directly, monthly mean climatologies of the SSH and geostrophic currents were calcu-
145 lated for the grid points along 6°E.

146 Monthly mean sea ice concentration (DiGirolamo et al., 2022) and velocity (Tschudi
147 et al., 2019) data at 25 km resolution were obtained from the National Snow and Ice Data
148 Centre. Monthly mean 10 m wind velocities were taken from the fifth generation of Eu-
149 ropean Center for Medium-Range Weather Forecasts atmospheric reanalyses (ERA5, Hers-
150 bach et al., 2023).

151 In addition, data from two sub-ice-shelf moorings installed under Fimbulisen (Hattermann
152 et al., 2012; Lauber, Hattermann, et al., 2023) were used. These moorings are located
153 along expected major deep inflow pathways of WDW into the cavity (M1 and M3, Fig.
154 1a) and have delivered temperature and velocity data at two depths each from 2009 to
155 2021.

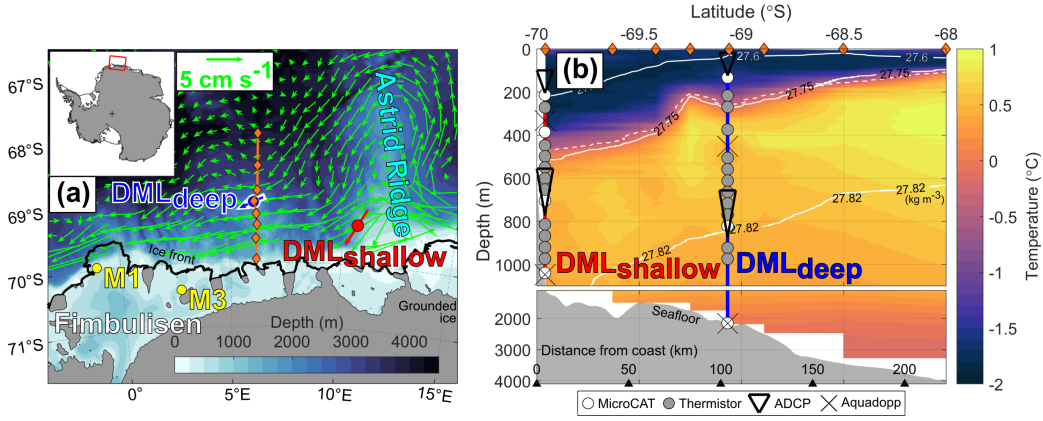


Figure 1. (a) Map of the study region. DML_{deep}/DML_{shallow} denote the open-ocean moorings, and M1/3 denote the sub-ice shelf moorings. The orange line shows the location of the CTD section in panel b, with stations marked by diamonds. Colors show the bathymetry (IBCSO v2, Dorschel et al., 2022). Arrows at the offshore mooring locations show the direction and strength of the depth- and time-averaged currents, and green arrows show the difference between April to July and August to March in surface geostrophic currents (Auger, Prandi, & Sallée, 2022). The scale arrow is valid for all arrows. (b) In-situ temperature of the CTD section indicated by the orange line in panel a. Solid white lines show selected isopycnals (potential density anomaly) and the single dashed white line shows the -0.3°C isotherm. Diamonds at the top are the station locations. The vertical blue line shows the location of DML_{deep}, and the vertical red line shows the isobath-projected location of DML_{shallow}.

3 Methods

To simplify investigations across the ASF/ASC, the data of DML_{shallow} were projected on the same isobath at the longitude of DML_{deep} (Fig. 1b). When doing this, we assumed that the flow (green arrows in Fig. 1a) is oriented along isobaths, as has been observed by Le Pailh et al. (2020) for the Weddell Sea and is corroborated by theoretical considerations of Isachsen et al. (2003). Therefore, for all velocity data, the component in the direction of the time- and depth-mean (red/blue arrow in Fig. 1a) will be shown in the following. The original location of DML_{deep} (105 km distance from the coast) and the projected location of DML_{shallow} (10 km distance from the coast) within the ASF with their instruments are shown in Fig. 1b.

Daily and monthly averages of the mooring time series were computed for use in subsequent analysis. Hydrographic properties like absolute salinity, conservative tem-

168 perature, and potential density were computed using the Gibbs Seawater Toolbox (McDougall
 169 & Barker, 2011). Temporary gaps in some of the ADCP bins due to seasonally reduced
 170 backscatter intensity were filled or extrapolated via a vertical linear regression of all avail-
 171 able bins.

172 Vertical profiles of temperature and salinity of the H18 data, provided as a func-
 173 tion of isobath, were projected on the bathymetry at 6°E, where the continental slope
 174 is less steep than at the original longitude of the climatology of 17°W. For this purpose,
 175 the bathymetry at 6°E was taken as a longitudinal average from 3°E to 9°E, based on
 176 IBCSO v2 data (Dorschel et al., 2022), to smooth out small-scale features.

177 Based on the general water mass distribution, the thermocline depth (TCD), i.e.
 178 the depth of the interface between WDW and WW, at the open-ocean moorings was de-
 179 fined as the depth of the -0.3°C isotherm after linear interpolation. Due to the verti-
 180 cally densely spaced thermistors (Fig. 1b), this depth was determined with an uncertainty
 181 of less than 50 m. The ASF slope was then calculated by combining the two thermocline
 182 depths:

$$slope_{ASF} = \frac{TCD_{shallow} - TCD_{deep}}{\Delta y} \quad (1)$$

183 Here, $TCD_{shallow}$ and TCD_{deep} are the thermocline depths for $DML_{shallow}$ and DML_{deep} ,
 184 respectively, and $\Delta y = 100$ km is the horizontal distance between the position of DML_{deep}
 185 and the projected position of $DML_{shallow}$. The same calculation was conducted for the
 186 H18 data over the corresponding isobaths.

187 The barotropic velocity, i.e. the depth-independent component, was estimated from
 188 the mooring data (UBT_{obs}) via averages over the depth ranges where the vertical gra-
 189 dient in velocity is the smallest:

$$UBT_{obs} = \overline{U_{obs, \Delta z}} \quad (2)$$

190 Here, $U_{obs, \Delta z}$ is the observed along-stream velocity of the lowermost 12 bins of the
 191 lower ADCP at each mooring (683-773 m at $DML_{shallow}$, 784-874 m at DML_{deep}), selected
 192 after inspecting the profiles. The bar indicates an average over this depth range. For com-
 193 parison, the barotropic velocity was also estimated from the auxiliary data by taking the
 194 difference between the A22 surface geostrophic velocity at 6°E ($UGEO_{A22}$, containing

195 both barotropic and baroclinic current components) and the surface baroclinic velocity
 196 from the H18 data (UBC_{H18} , defined in Eqn. 5) after binning them on the same grid:

$$UBT_{H18A22} = UGEO_{A22} - UBC_{H18} \quad (3)$$

197 From the resulting time-latitude field of velocity, time series at the mooring iso-
 198 baths were extracted.

199 The near-surface baroclinic velocity, i.e. the depth-varying component, was esti-
 200 mated from the mooring data (UBC_{obs}) by subtracting UBT_{obs} from the measured ve-
 201 locity at the uppermost ADCP bin (100 m at $DML_{shallow}$, 20 m at DML_{deep}):

$$UBC_{obs} = U_{obs} - UBT_{obs} \quad (4)$$

202 Here, U_{obs} is the observed along-stream velocity at the uppermost ADCP bin. The
 203 baroclinic velocity was also calculated from the H18 climatology for 6°E (UBC_{H18}) us-
 204 ing the thermal wind equation:

$$UBC_{H18}^i = \frac{\Delta z}{\rho_0 f} \frac{\rho_{j+1}^i - \rho_j^i}{\Delta y} + UBC_j^{i-1} \quad (5)$$

205 Here, $\Delta z = 20$ m is the depth increment, $\rho_0 = 1028 \text{ kg m}^{-3}$ is a background den-
 206 sity, f is the Coriolis parameter, i is the upward increasing depth index, j is the north-
 207 ward increasing meridional index, and $\Delta y = 4$ km is the meridional increment. Zero
 208 velocity was assumed at the bottom or the lowest depth with data available. From the
 209 resulting depth-isobath-time field, time series were extracted over the isobaths and at
 210 the upper ADCP bin depths of DML_{deep} and $DML_{shallow}$ to compare to UBC_{obs} .

211 Sea ice concentration and velocity, as well as wind data were interpolated on a com-
 212 mon polar stereographic grid and combined to yield an estimate of the ocean stress (Martin
 213 et al., 2016; Dotto et al., 2018):

$$\vec{\tau} = \alpha \vec{\tau}_{ice-water} + (1 - \alpha) \vec{\tau}_{air-water} \quad (6)$$

214 with

$$\vec{\tau}_{ice-water} = \rho_{water} C_{iw} \left| \vec{U}_{ice} \right| \vec{U}_{ice} \quad (7)$$

$$\vec{\tau}_{air-water} = \rho_{air} C_d \left| \vec{U}_{air} \right| \vec{U}_{air} \quad (8)$$

215 Here, α is the sea ice concentration, $\rho_{air} = 1.25 \text{ kg m}^{-3}$ is the background den-
 216 sity of air, $\rho_{water} = 1028 \text{ kg m}^{-3}$ is the background density of seawater, \vec{U}_{ice} is the hor-
 217 izontal sea ice velocity, \vec{U}_{air} is the 10 m horizontal wind and $C_d = 1.25 \times 10^{-3}$ and $C_{iw} =$
 218 5.50×10^{-3} (Tsamados et al., 2014) are the drag coefficients for the air-water and ice-
 219 water interface, respectively. Stresses from the ocean currents on the ice from below were
 220 not included here, possibly creating biases close to the coast where the sea ice velocity
 221 is similar to the ocean velocity (Stewart et al., 2019). Le Paih et al. (2020), however, show
 222 that the ocean stress in this region can still be qualitatively valid despite neglecting the
 223 ocean currents. The curl was calculated from the ocean stress, with positive (negative)
 224 values indicating downwelling (upwelling) favorable conditions.

225 To assess the relationship between the ASF/ASC dynamics and inflow of mWDW
 226 below Fimbulisen, the data from the lower M1 and M3 instruments (at 540 m and 450 m,
 227 respectively) close to the seabed were used, referred to as M1_{lower} and M3_{lower} hereafter.
 228 The velocity was rotated to be oriented into the cavity along the bathymetry, that is -30°
 229 at M1_{lower} and -120° at M3_{lower} (0° is directed toward the east and negative values in-
 230 dicate a clockwise rotation).

231 4 Results

232 4.1 Mooring Observations

233 4.1.1 Hydrography

234 The CTD section from December 2020 and January 2021 (Fig. 1b) shows the typ-
 235 ical southward down-sloping isopycnals of the ASF and the offshore core of the WDW
 236 at the northern edge of the section at a depth of around 300-400 m. The section repre-
 237 sents a snapshot of the ASF during summertime.

238 A Hovmöller diagram of temperature at DML_{shallow} (Fig. 2a) shows a layer of cold
 239 water with temperatures down to -1.9°C over a layer of warm water with temperatures
 240 up to 1°C . The thermocline depth (-0.3°C isotherm) shows a systematic seasonality,
 241 deepening between April and June to 500 m, and shoaling between July and March to

242 200 m. At DML_{deep} , the thermocline is on average 100 m shallower than at DML_{shallow}
 243 (Fig. 2c) and deepens between June and December to 400 m, i.e. it reaches its maximum
 244 depth six months later compared to DML_{shallow} . In 2020, the deepening is interrupted
 245 by a period of shoaling in October/November. The thermocline continues to shoal to 200 m
 246 from January to May, and reaches its minimum depth two months later compared to DML_{shallow} .
 247 The warmest WDW is seen at both sites when the thermocline is shallowest.

248 The upper-ocean water masses (of which the densities are almost entirely deter-
 249 mined by salinity) at DML_{shallow} are characterized in a temperature-salinity (T-S) di-
 250 agram (Fig. 3a): the upper water mass is cold ($\approx -1.8^\circ\text{C}$) and fresh ($\approx 34.5 \text{ g kg}^{-1}$)
 251 WW, transforming into mWDW by mixing with the lower water mass which is warm
 252 ($\approx 1^\circ\text{C}$) and saline ($\approx 34.8 \text{ g kg}^{-1}$) WDW. Oxygen (colors in Fig. 3 and time series
 253 in Fig. S1 in Supporting Information S1) is a measure of the origin of the water masses.
 254 The freshest and oxygen-richest WW is observed at the uppermost MicroCAT (210 m)
 255 at the time of the deepest thermocline in winter in June. This water mass is similar to
 256 Eastern Shelf Water, a mix between ASW and WW. The observed WW in June 2019
 257 is almost 0.1 g kg^{-1} fresher and richer in oxygen than in June 2020. During the period
 258 of thermocline shoaling from July onward, mWDW gradually appears. The most saline,
 259 warm, and oxygen-poor mWDW is observed in March when the thermocline is shallow-
 260 est (see also Fig. 2a). At the uppermost MicroCAT (130 m) at DML_{deep} , the WDW shows
 261 similar properties as at DML_{shallow} , but the WW is generally more saline (Fig. 3b). A
 262 first seasonal salinity minimum and oxygen maximum are observed in June 2019. Af-
 263 ter that, temperature and salinity first increase toward mWDW, but then decrease back
 264 to WW. This yields a second seasonal salinity minimum and oxygen maximum at the
 265 time of the deepest thermocline in December 2019. During the period of thermocline shoal-
 266 ing, the water mass properties change toward mWDW until May 2020. After that, when
 267 the thermocline deepens, WW appears again, which is 0.05 g kg^{-1} more saline and has
 268 a lower oxygen concentration than in 2019. This is similar to the higher salinities and
 269 reduced oxygen observed at DML_{shallow} in 2020 (relative to 2019).

270 The observed seasonal deepening and freshening of the WW layer at DML_{shallow}
 271 (Fig. 2a) is attributed to the wind-driven accumulation of ASW at the coast (Zhou et
 272 al., 2014; Hattermann, 2018): summer sea ice melt between September and February (Fig.
 273 4a) adds freshwater to form ASW. The latter is downwelled at the coast due to the pre-
 274 vailing easterly winds, explaining the salinity minimum and oxygen maximum at 210 m

275 at DML_{shallow} in June 2019 and 2020 (Fig. 3a and 4b) and the deepest thermocline one
276 month later in July (Fig. 4c). Sea ice formation between March and August (Fig. 4a)
277 releases brine into the upper ocean and leads to a salinity increase between July and Septem-
278 ber. With temperatures almost at the freezing point and oxygen close to its maximum
279 value, this indicates that convection takes place down to 210 m depth during this period
280 at DML_{shallow} in 2019 (box in Fig. 3a). In 2020, the temperature is higher and the oxy-
281 gen concentration is lower during the sea ice formation period, suggesting that convec-
282 tion did not reach down to this depth.

283 We also identify a period of convection at DML_{deep} : From June to August 2020,
284 the water mass evolution from mWDW to similarly cold, but more saline and less oxygen-
285 rich WW than in 2019 shows a mixing between mWDW and WW salinified by convec-
286 tion (box in Fig. 3b). In October/November 2020, the increase in temperature and salin-
287 ity (off the direct mixing line toward WDW) and decrease in oxygen indicate that the
288 convection reached through the thermocline, mixing WDW upward. This is neither ob-
289 served in 2019 nor at DML_{shallow} . At 130 m at DML_{deep} , the different seasonal cycles
290 in salinity (Fig. 4b) and thermocline depth (Fig. 4c) than at DML_{shallow} indicate that
291 local downwelling of ASW does not control the seasonal hydrography here: the salinity
292 minimum in December cannot be explained by local surface freshwater input, as brine
293 release during the freezing season from March to August (Fig. 4a) would increase the
294 salinity, and freshwater from sea ice melt would cause a salinity minimum at the end (i.e.
295 in March), not the beginning of the melt season. The drivers of the hydrographic sea-
296 sonality at DML_{deep} will be explored in section 4.2.

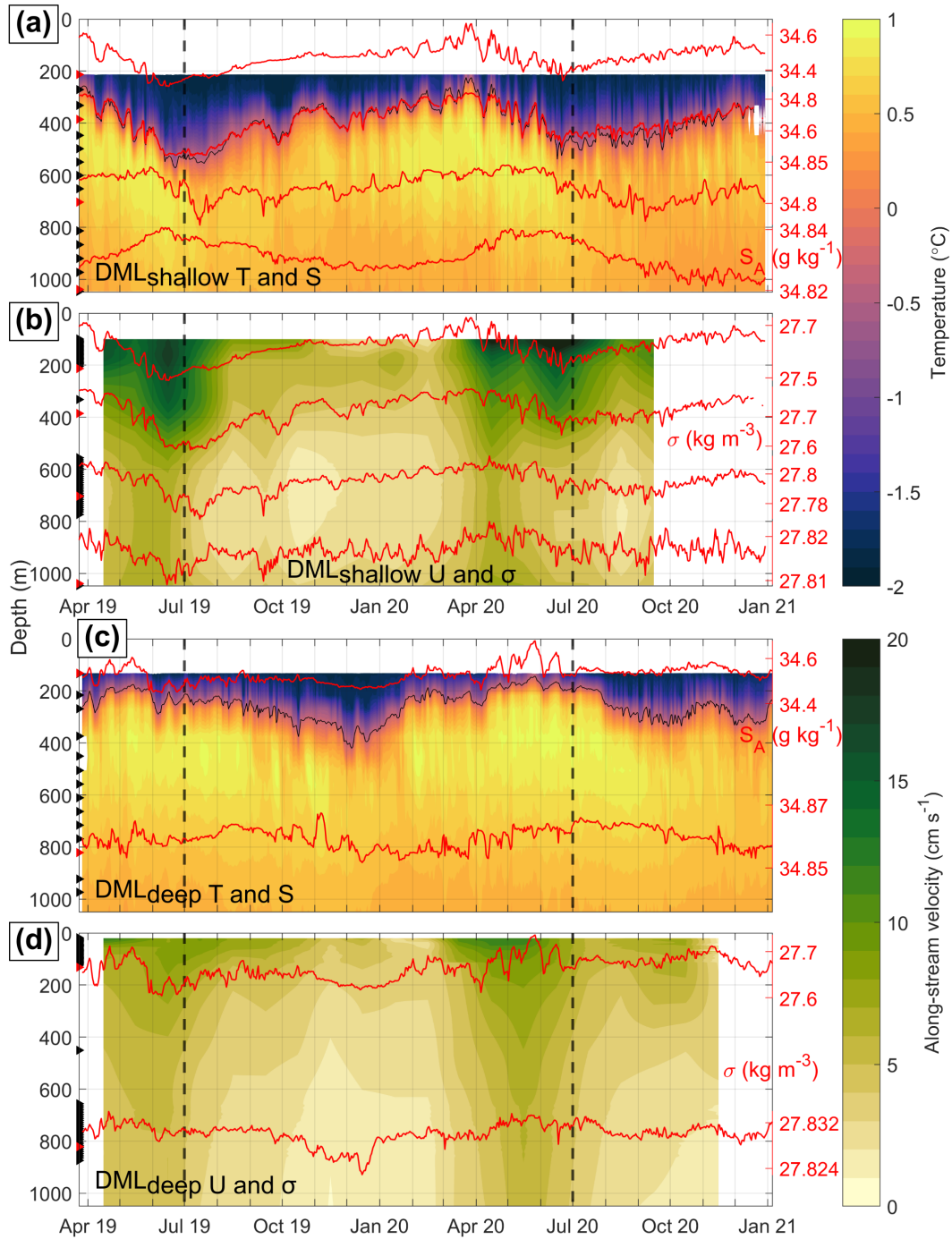


Figure 2. (a) Hovmöller diagram of daily averaged in-situ temperature at DML_{shallow}. The black contour indicates the -0.3°C isotherm. Black triangles denote the depths of temperature measurements. Red lines show daily averaged time series of absolute salinity (right axes) for the depths marked with red triangles. (b) Hovmöller diagram of monthly averaged along-stream velocity at DML_{shallow}. Black triangles denote the depths of velocity measurements. Red lines show daily averaged time series of potential density anomaly (right axes) for the depths marked with red triangles. (c) Same as a, but for DML_{deep}. (d) Same as b, but for DML_{deep}. In c and d, the y-axis has been cut off at the bottom depth of $\underline{DML}_{shallow}$ for better comparability.

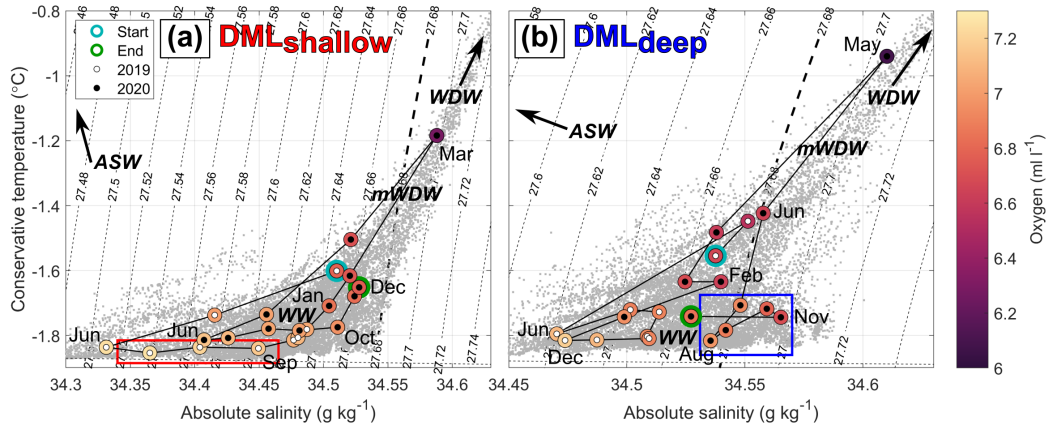


Figure 3. T-S diagrams with dissolved oxygen of the upper MicroCAT at (a) $DML_{shallow}$ (210 m) and (b) DML_{deep} (130 m). Grey dots are the fully resolved hourly data, and colored dots are the monthly averaged data. Black lines connect the monthly points. The boxes show potential periods of convection. The thick black dotted line indicates the 27.68 kg m^{-3} isopycnal for better comparability between the two panels, as their x-axis ranges differ.

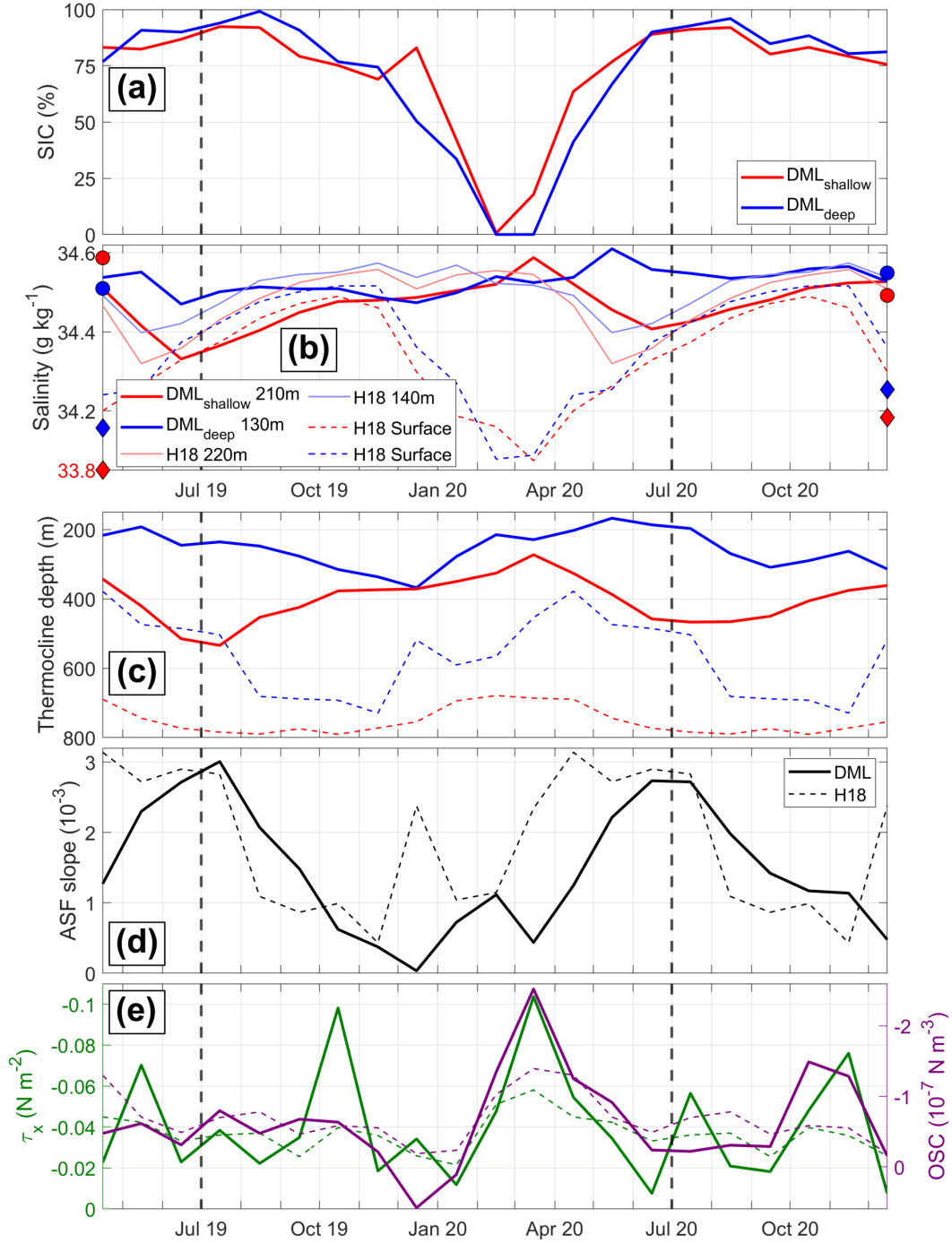


Figure 4. Monthly means of: (a) Sea ice concentration at both open-ocean mooring locations. (b) Salinity observed at the uppermost MicroCAT at both moorings (210 m at DML_{shallow}, 130 m at DML_{deep}), salinity from the H18 climatology over similar isobaths and at similar depths, and salinity from the H18 climatology over similar isobaths at the surface. Dots/diamonds indicate the salinity at the MicroCAT depth/surface from the CTD profiles of the deployment and recovery cruises. The red diamond on the left is off-scale. (c) Thermocline depth defined as the -0.3°C isotherm at both moorings and from the H18 climatology over similar isobaths. (d) ASF slope estimated from the thermocline depths from panel c for the mooring data and the H18 climatology (Eqn. 1). (e) Regional zonal ocean stress (left axis) and ocean stress curl (right axis), averaged over $0-15^{\circ}\text{E}$ and $69.5-70^{\circ}\text{S}/67-69.5^{\circ}\text{S}$, respectively (solid lines), along with their climatology (2010-2021, dashed lines).

297

4.1.2 Velocity

298

299

300

301

302

303

304

305

306

307

308

At DML_{shallow} , monthly mean velocities (Fig. 2b) show a surface-intensified current, which at 100 m is strongest in June in both years (20 cm s^{-1}). At 600-800 m, the velocity shows a vertical minimum throughout the length of the record. Toward the bottom, the velocity intensifies by 2 cm s^{-1} . The vertical gradient, i.e. the baroclinic part, becomes more apparent in profiles when averaged over specific months (Fig. 5a): Toward the surface, the strongest vertical shear is observed in June. Below 500 m, there is smaller seasonal variability in the gradient. At DML_{deep} (Fig. 2d), velocities are generally smaller than at DML_{shallow} with maximum values of 10 cm s^{-1} at 20 m observed in May/June 2019 and April/May 2020. In contrast to DML_{shallow} , the velocity at DML_{deep} continuously decreases toward the bottom (Fig. 5b). The seasonality of the upper-ocean vertical shear is weaker than at DML_{shallow} and strongest in March.

309

310

311

312

313

314

315

316

317

318

The estimated barotropic component (UBT_{obs}) at DML_{shallow} (Fig. 6b) is maximum (6 cm s^{-1}) in May/June 2019 and April 2020. At DML_{deep} , the values are slightly smaller and the maximum occurs one month later than at DML_{shallow} in 2020, but not in 2019 when there is zero lag. The baroclinic velocity (UBC_{obs}) at DML_{shallow} at 100 m depth (Fig. 6d) shows a first seasonal maximum (12 cm s^{-1}) in April 2019. In 2020, a local maximum in April is followed by a higher seasonal maximum (20 cm s^{-1}) in June. The baroclinic velocity is close to 0 cm s^{-1} from December 2019 to February 2020. At DML_{deep} at 20 m depth (Fig. 6e), a maximum baroclinic velocity of 7 cm s^{-1} is observed in April in both years. Seasonal minima close to 0 cm s^{-1} occur in January and December 2020.

319

320

321

322

323

324

325

326

327

328

The ASF slope, derived from the thermocline depths at DML_{shallow} and DML_{deep} (Eqn. 1), is steepest in June/July (Fig. 4d). In 2020, this is around the same time as the maximum near-surface UBC_{obs} at DML_{shallow} (Fig. 6d), consistent with thermal wind balance. In 2019, however, a distinct maximum in ASF slope is found in July but no clear maximum in baroclinic velocity is observed (Fig. 6d). The weakest ASF slope occurs in December when the thermocline depths at the two moorings become equal due to a shoaling at DML_{shallow} and a deepening at DML_{deep} (Fig. 4c-d). Accordingly, UBC_{obs} at DML_{shallow} is close to its seasonal minimum between December and February (Fig. 6d). Despite some coinciding features, the ASF slope and the baroclinic velocities at the moorings are not directly comparable, since (i) most of baroclinic velocity shear occurs above the thermo-

329 cline (Fig. 5), and (ii) the (assumed) linear ASF slope between the moorings may not
 330 represent the local ASF slope at the mooring locations.

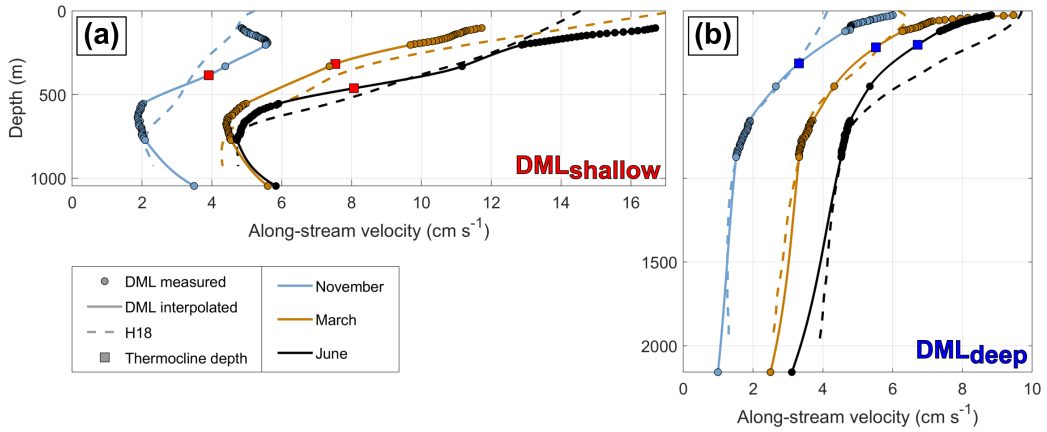


Figure 5. (a) Profiles of along-stream velocity at (a) $DML_{shallow}$ and (b) DML_{deep} , averaged over a three-month-window centered at three selected months. The velocities are vertically interpolated via a shape-preserving piecewise cubic interpolation. Additionally, the averages of the zonal baroclinic velocity profiles over the same time interval and for similar isobaths calculated from the H18 climatology are shown. For better comparability, the depth-constant UBT_{obs} has been added to the H18 profiles.

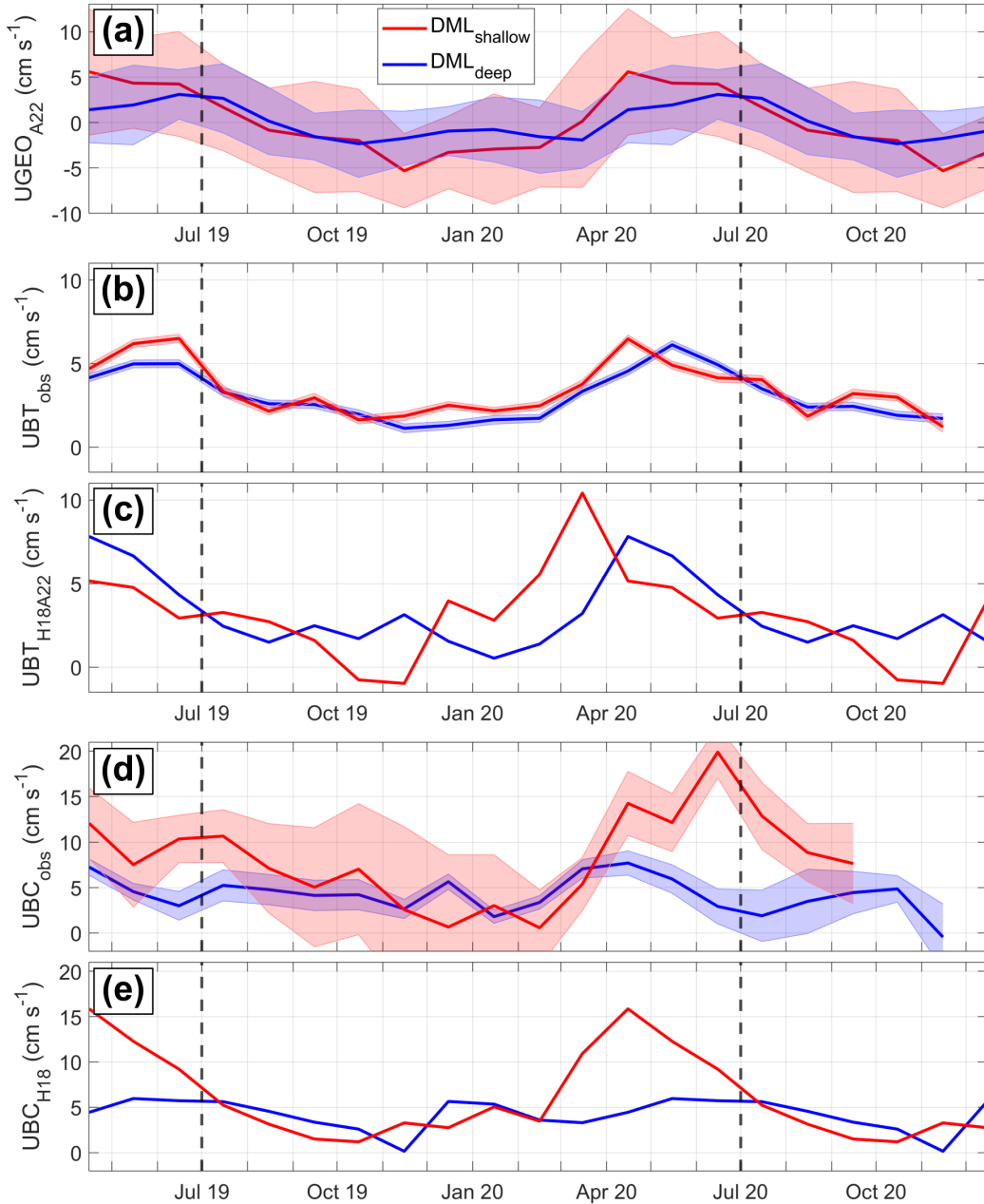


Figure 6. (a) Surface geostrophic velocity anomaly from A22 interpolated on the DML_{shallow} and DML_{deep} locations. (b) Barotropic velocity derived from mooring data. (c) Barotropic velocity derived from A22 and H18 data, obtained over the respective mooring isobaths. Shown are anomalies plus the respective time-mean of panel b. (d) Baroclinic velocity derived from mooring data at the uppermost ADCP bin depth (100 m at DML_{shallow}, 20 m at DML_{deep}). (e) Baroclinic velocity derived from the H18 climatology, taken over the mooring isobaths at the same depths as panel d. Details about the calculation of the error bars are given in Text S1 in Supporting Information S1.

331

4.1.3 Ocean Stress Forcing

332

333

334

335

336

337

338

339

To investigate the extent to which ocean stress contributes to the variability of the ASC at the moorings, we differentiate between regional ($0\text{--}15^\circ\text{E}$, $67\text{--}70^\circ\text{S}$) and remote upstream ($0\text{--}60^\circ\text{E}$ and $50\text{--}70^\circ\text{S}$), ocean stress and its curl. We further differentiate between the shallow ($< 1000\text{ m}$, more influenced by zonal ocean stress) and deep ($> 1000\text{ m}$, more influenced by ocean stress curl) regime suggested by Auger, Sallée, et al. (2022). We note that for both local and remote ocean stress, the modulation of the wind stress by sea ice causes the seasonal maximum in ocean stress to occur one month earlier than the maximum in wind stress.

340

341

342

343

344

345

346

347

348

349

350

351

352

353

354

355

356

357

358

Monthly mean regional ocean stress forcing does not show a distinct seasonal cycle during the mooring period, in contrast with the 12-year mean seasonality (Fig. 4e). The zonal ocean stress (meridionally averaged over $69.5\text{--}70^\circ\text{S}$, i.e. over the continental slope) is westward and strongest in October 2019 and March 2020. In April 2020, thermocline deepening starts at $\text{DML}_{\text{shallow}}$ (Fig. 4c), and a local maximum is found in the baroclinic velocity (Fig. 6e) at $\text{DML}_{\text{shallow}}$. This is consistent with coastal downwelling due to stronger onshore Ekman transport. However, no strong regional ocean stress occurred in early 2019 prior to the mooring deployment (not shown). In addition, the regional ocean stress maximum in October 2019 does not coincide with a thermocline deepening. The monthly mean regional ocean stress curl (meridionally averaged over $67\text{--}69.5^\circ\text{S}$, i.e. off the continental slope) is close to zero most of the time but has a clear maximum between February and April 2020 (Fig. 4e). Estimated Ekman upwelling of $w_{Ek} = \frac{OSC}{\rho_0 f} = 4\text{ m month}^{-1}$ (with ocean stress curl $OSC = -0.2 \times 10^{-7}\text{ N m}^{-3}$, background density $\rho_0 = 1028\text{ kg m}^{-3}$, Coriolis parameter $f = -1.36 \times 10^{-4}\text{ s}^{-1}$) can, however, not explain the thermocline shoaling and upper-ocean salinity increase observed at DML_{deep} between January and May 2020 (Fig. 4b-c). Overall, the poor agreement between UBC_{obs} at $\text{DML}_{\text{shallow}}$ and regional ocean stress forcing indicates that the latter is not the main driver of the baroclinic velocity seasonality. This will be further investigated in section 4.2.

359

360

361

362

363

To investigate the forcing of the barotropic ASC, we correlate UBT_{obs} at $\text{DML}_{\text{shallow}}$ with zonal ocean stress (Fig. 7a) and UBT_{obs} at DML_{deep} with ocean stress curl (Fig. 7b). The highest negative correlations are found along the East-Antarctic coast at $30\text{--}60^\circ\text{E}$ with UBT_{obs} lagging the ocean stress by one month. The patterns are similar when correlating UBT_{obs} at DML_{deep} with zonal ocean stress or UBT_{obs} at $\text{DML}_{\text{shallow}}$ with ocean

364 stress curl. Therefore, the bands of high correlation are independent of the method dif-
 365 ferentiating the regimes from Auger, Sallée, et al. (2022). In contrast to the regional forc-
 366 ing (Fig. 4e), the remote ocean stress and its curl exhibit a distinct seasonal cycle dur-
 367 ing the mooring period over the areas of highest correlations along East Antarctica, sim-
 368 ilar to the multi-year climatology (Fig. 7c). Strong westward ocean stress and negative
 369 ocean stress curl seasonally increase the cross-shore SSH gradient in autumn (March-May).
 370 This gradient travels westward through coastal Kelvin waves (Webb et al., 2022), explain-
 371 ing the seasonal variability of the barotropic flow at the moorings (Fig. 6b). This can
 372 also explain the observed interannual variability like the maximum occurring later in 2019
 373 than in 2020 in remote ocean stress (Fig. 7c) and UBT_{obs} (Fig. 6b).

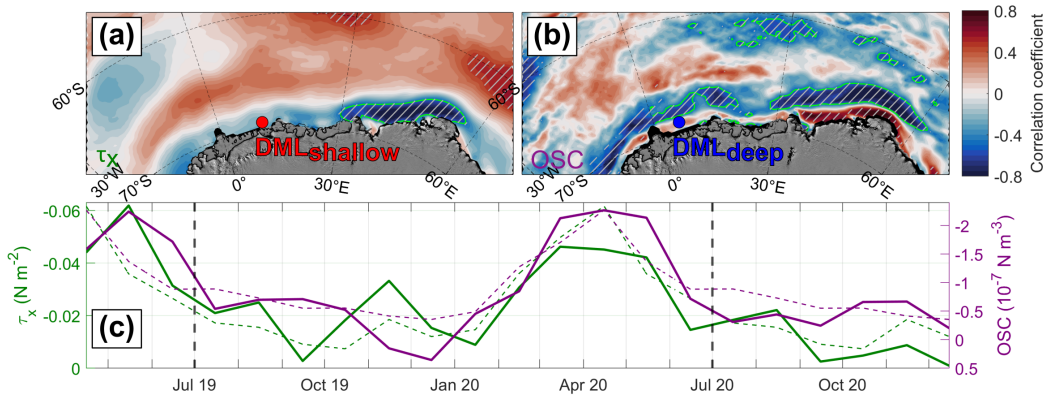


Figure 7. Correlation maps of (a) barotropic velocity UBT_{obs} at DML_{shallow} from Fig. 6b, lagged by one month, and zonal ocean stress, and (b) barotropic velocity UBT_{obs} at DML_{deep} from Fig. 6b, lagged by one month, and ocean stress curl at every grid point. Hatched areas indicate a significance of at least 95 %, and green lines mark areas of a correlation of at least -0.5 east of the prime meridian. The background satellite image is taken from Haran et al. (2018). (c) Zonal ocean stress (left axis) and ocean stress curl (right axis) averaged over 0–60°E and 50–70°S where the correlations from panels a and b, respectively, are at least -0.5, along with their climatology (2010-2021, dashed lines).

374 4.2 Seasonal Cycle from Auxiliary Data Sets

375 Our new mooring data show different processes governing the seasonal hydrographic
 376 and dynamic variability at DML_{shallow} and DML_{deep}. As we will demonstrate in this sec-
 377 tion, these processes are consistent with the H18 data, providing information above the
 378 uppermost moored instruments and over multiple isobaths. We next use these data to

investigate the forcing of the baroclinic seasonality and the delay in salinity and thermocline depth seasonality observed between DML_{shallow} and DML_{deep} in more detail.

4.2.1 The Role of ASW for the Hydrographic Seasonality

In both the mooring records (Fig. 4b) and the H18 data set (Fig. S2 in Supporting Information S1), the seasonal subsurface salinity minimum occurs later over deeper isobaths than over shallow isobaths. For the mooring isobaths, the delay in the H18 data increases from zero at the surface, where the salinity is determined directly by freshwater input from sea ice melt, to five months at 400 m depth. The freshwater content integrated down to this depth illustrates that the offshore delay in salinity minimum is a robust feature across multiple isobaths (Fig. 8a): in March, fresh ASW accumulates at the coast, and in the subsequent months, the ASW spreads and deepens offshore, delaying the timing of maximum offshore freshwater content well into the freezing season. This is most pronounced over isobaths shallower than 2000 m. As the offshore ASW spreading and deepening displaces WW to greater depths, the deepest thermocline follows the highest freshwater content and thus shows a similar offshore delay (Fig. S3 in Supporting Information S1). This is consistent with the mooring observations and explains the different seasonalities of and the robust link between salinity and thermocline depth over the two isobaths (Fig. 2a/c).

The seasonal offshore spreading and deepening of ASW moves the secondary front and the ASF, causing the maximum surface baroclinic velocity from H18 to move toward deeper isobaths throughout the season (Fig. 8b). This is again clearest over isobaths shallower than 2000 m. Consequently, over the mooring isobaths, time series of UBC_{H18} (Fig. 6e) agree well with UBC_{obs} (Fig. 6d), apart from the maximum occurring two months later at the DML_{shallow} mooring in 2020.

Next, we use the H18 data to estimate the contribution of the baroclinic component to the surface geostrophic velocity from A22. At the location of DML_{shallow} , the surface geostrophic velocity shows a seasonal amplitude of 10 cm s^{-1} and a maximum in April (Fig. 6a). At the DML_{deep} location, the seasonal amplitude is 5 cm s^{-1} and the maximum occurs in June (Fig. 6a). This delay becomes clearer in time-latitude space, in which the surface geostrophic velocity seasonality from A22 at 6°E also shows an offshore delay (Fig. 8c). This time lag, however, is somewhat smaller than in the H18 surface baroclinic velocity (Fig. 8b). The barotropic velocity anomaly (UBT_{H18A22}) is then

411 estimated as the difference between the A22 surface geostrophic and H18 surface baro-
 412 clinic velocity (Fig. 8d). A moderate offshore delay is still visible in the seasonal cycle
 413 of UBT_{H18A22} , with a phase shift of one to two months between the mooring sites (Fig.
 414 6d). Given the uncertainties in both data sets that UBT_{H18A22} is derived from, we can-
 415 not conclude if this remaining phase shift is realistic (see section 5).

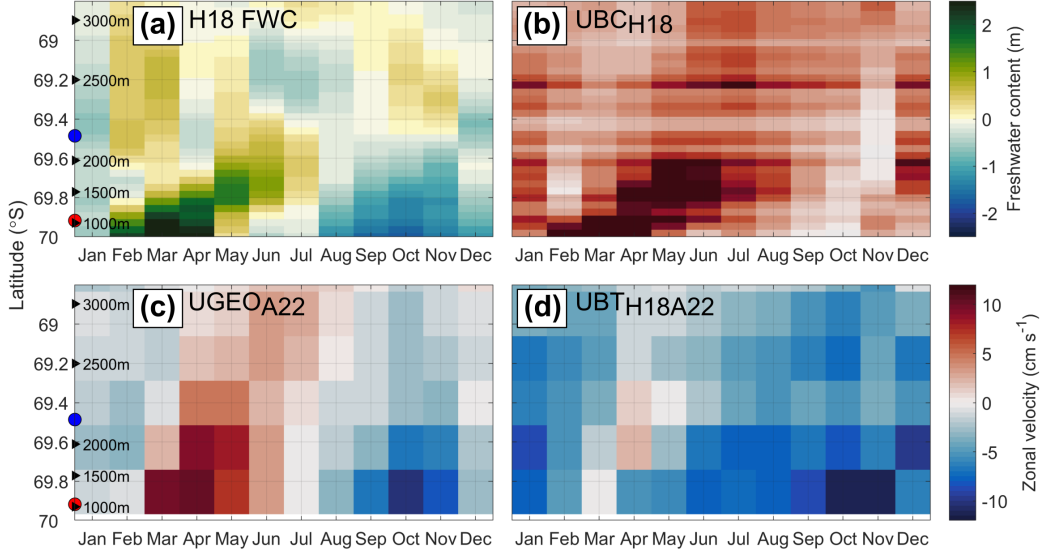


Figure 8. Hovmöller diagrams of (a) depth-integrated freshwater content within the upper 400 m referenced to a salinity of 34.6 g kg^{-1} from H18, (b) zonal surface baroclinic velocity derived from H18, (c) zonal surface geostrophic velocity anomaly from A22 at 6°E , (d) zonal barotropic velocity anomaly obtained by taking panel c minus panel b. The red/blue dots indicate the isobath of $DML_{\text{shallow}}/DML_{\text{deep}}$.

4.2.2 Implications for ASF/ASC Dynamics

416
 417 The coastal freshwater content maximum in March (Fig. 8a) and the resulting sur-
 418 face baroclinic velocity (Fig. 8b) cannot originate from seasonally increased ocean stress
 419 (Fig. 4e). Instead, it is caused by the freshening of upper-ocean water masses through
 420 seasonal sea ice melt and their concurrent accumulation at the coast. These results align
 421 with observed seasonal cycles in hydrography (Fig. 2a and 4b-d) and baroclinic veloc-
 422 ity (Fig. 5a, Fig. 6d) at DML_{shallow} , despite a weak seasonality in local zonal ocean stress
 423 (Fig. 4e). Therefore, the mooring and H18 data are consistent in that seasonal freshwa-
 424 ter input from sea ice melt is an essential forcing of the surface baroclinic velocity sea-

425 sonality and magnitude, independent of any seasonality in ocean-stress-driven coastal
426 downwelling.

427 The velocity shear toward the surface in March and June at the upper ADCPs of
428 both moorings (reaching 110 m higher than the uppermost MicroCATs, Fig 5) indicates
429 the presence of the secondary front between ASW and WW at the sites. Although the
430 strongest upper-ocean velocity shear at DML_{shallow} is found in March in the H18 data,
431 and in June in the mooring data, the shapes of the observed velocity profiles generally
432 agree with the ones from H18 over similar isobaths. In addition, the offshore delay in ther-
433 mocline depth maximum and salinity minimum at DML_{deep} is consistent between the
434 mooring and H18 data (Fig. 4b-c, Fig. 8a, Fig. S3 in Supporting Information S1). We
435 thus infer that the offshore spreading and deepening of ASW identified in Fig. 8a also
436 takes place at the mooring longitude of 6°E .

437 We propose that eddy overturning, as demonstrated by Si et al. (2023) using an
438 eddy-resolving model, drives the observed offshore delay in seasonal freshwater content
439 (Fig 8a): after the phase of the freshest ASW at the coast in March and with slacken-
440 ing local and remote ocean stress forcing, eddy overturning acts to relax the secondary
441 front, consistent with large eddy growth rate estimates from January to June (Hattermann,
442 2018). Thereby, the fresh signal spreads and deepens offshore during the course of the
443 following months, causing the observed delay in offshore thermocline depth (Fig. 4c) and
444 salinity (Fig. 4b) seasonality. Eddy overturning also transports salty WW from offshore
445 toward the coast, contributing to the decrease in coastal freshwater content after June
446 (Fig. 8a) in addition to convection.

447 We also identify some differences between the mooring records and the H18 data:
448 the thermocline in the H18 data is consistently 200 m deeper than in the mooring ob-
449 servations (Fig. 4c). As a result of this vertical offset, the seasonal salinity minimum ob-
450 served in December at 130 m and 810 m at DML_{deep} (Fig. 2c) shows up in November in
451 the H18 data below 400 m, but not above (Fig. S2b in Supporting Information S1). In
452 addition to this vertical offset, the seasonal extremes of salinity at DML_{shallow} (Fig. 4b),
453 of the thermocline depth (Fig. 4c) and of the ASF slope (Fig. 4d) occur one to two months
454 earlier in the H18 data than in the mooring observations. Advection of water masses within
455 the ASC, as suggested by Graham et al. (2013), may explain the alongshore thermocline
456 deepening, but not the delayed seasonal extremes at 6°E compared to 17°W . With the
457 data sets being obtained in different years, we cannot conclude if the described offsets

458 are a robust feature or the result of interannual variability, and if alongshore advection
 459 plays a role.

460 **4.3 ASF/ASC Variability and Inflow below Fimbulisen**

461 To assess the role of the variability of the ASF/ASC system on the deep inflow of
 462 mWDW into the cavity of Fimbulisen, we now compare the open-ocean mooring data
 463 from $DML_{\text{shallow}}/DML_{\text{deep}}$ with the concurrent sub-ice-shelf mooring data from $M1_{\text{lower}}$
 464 and $M3_{\text{lower}}$ (Fig. 1a). The open-ocean moorings are roughly 200 km upstream of Fim-
 465 bulisen, but supported by the agreement between the the mooring and H18 data, we as-
 466 sume that the seasonality does not change considerably over this distance.

467 Mooring M1 is located on the main sill that connects the cavity to the open ocean
 468 (Fig. 1a). This sill is at 560 m depth and is directed across the continental slope. Here,
 469 the velocity alternates seasonally between a period of flow into the cavity between July/August
 470 and February and a period of flow out of the cavity between March and June/July (Fig.
 471 9a). The seasonality of the cavity inflow at $M1_{\text{lower}}$ anticorrelates with the ASC strength:
 472 the current is directed into the cavity during periods of a weak barotropic and baroclinic
 473 (at 330 m, i.e. the depth of the velocity measuring instrument closest to the WDW core
 474 at DML_{shallow}) ASC, while it is directed out of the cavity during periods of a strong ASC.
 475 At $M3_{\text{lower}}$, located in the east of Fimbulisen on a second sill that is 480 m deep and di-
 476 rected more along the continental slope (Fig. 1a), the connection between inflow and the
 477 ASC strength is the opposite, i.e. inflow occurs during periods of a strong ASC, and out-
 478 flow - or weak inflow - during periods of a weak ASC (Fig. 9a).

479 The temperature at $M1_{\text{lower}}$ (Fig. 9b) does not show a clear seasonality during the
 480 mooring period, and we do not find a significant correlation to the seasonally varying
 481 thermocline depth (Fig. 9c) on time scales from days to months. Instead, the $M1_{\text{lower}}$
 482 temperature lies around the surface freezing point most of the time, showing irregular
 483 episodes with higher temperatures of up to almost 0 °C. These temperature extremes
 484 are not, as one would expect, associated with a particularly shallow thermocline and high
 485 WDW temperatures at DML_{shallow} . Similarly, the cavity temperature at $M3_{\text{lower}}$ does
 486 not correlate with the thermocline depth: the lowest temperatures occur shortly after
 487 the minimum in thermocline depth in March 2020. Interestingly, despite the opposing
 488 inflow and outflow velocities at the two sub-ice-shelf mooring sites, peak temperatures
 489 occur simultaneously at $M1_{\text{lower}}$ and $M3_{\text{lower}}$ in August/September 2019, suggesting a

490 forcing driving mWDW inflow over a larger area. At most times, however, the temper-
 491 atures at $M1_{lower}$ and $M3_{lower}$ appear to be unrelated. Further interpretations of the ob-
 492 served variability below Fimbulisen with regard to the ASC are given in section 5.

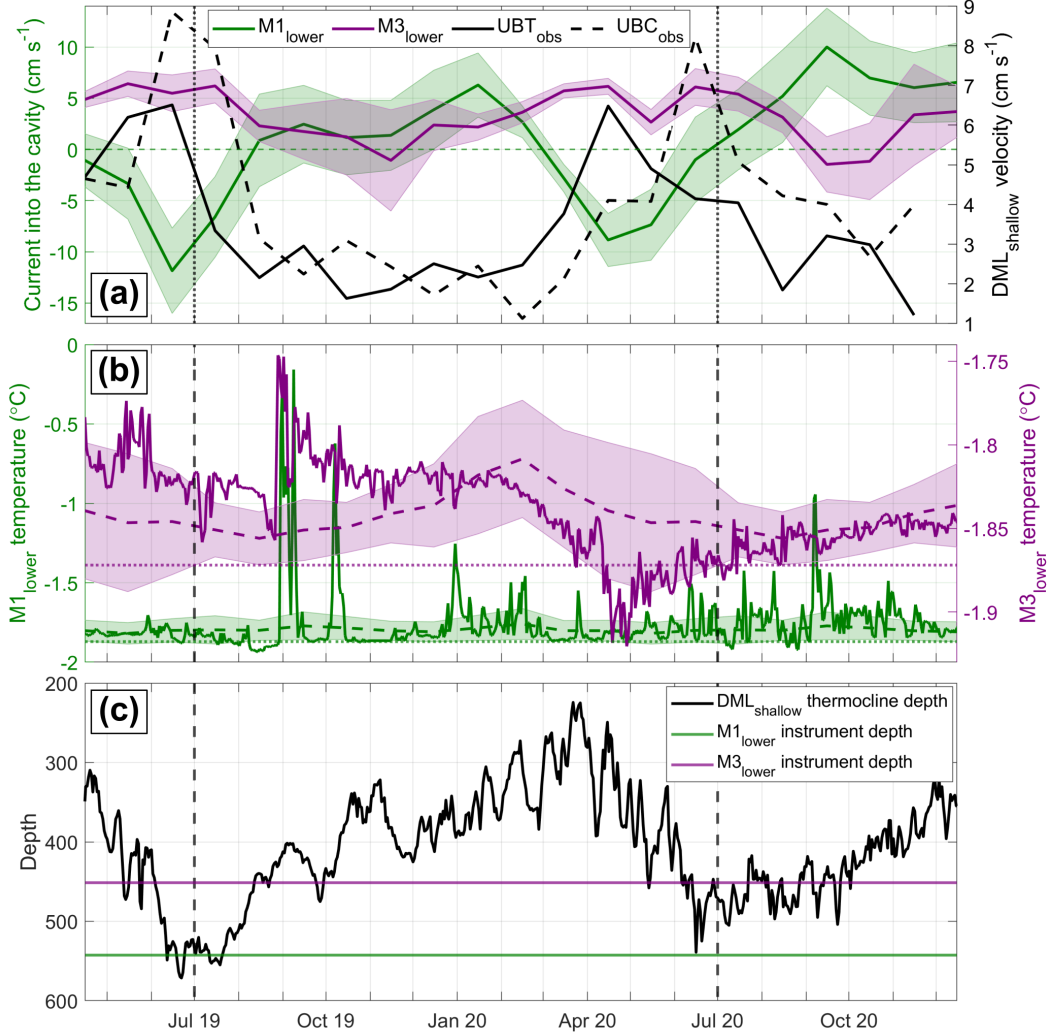


Figure 9. (a) Monthly averages of the currents at $M1_{lower}$ and $M3_{lower}$ (left axis), rotated into the cavity as described in section 3, together with UBT_{obs} (same as the red line in Fig. 6b) and UBC_{obs} at 330 m depth at $DML_{shallow}$ (right axis). Envelopes denote the standard deviation of the monthly climatology (2010-2021). (b) Daily averages of in-situ temperature at $M1_{lower}$ (left axis) and $M3_{lower}$ (right axis, solid lines), along with their monthly climatology and standard deviation (2010-2021, dashed lines and envelope, respectively). Dotted lines are the surface freezing temperature for a salinity of 34.4 g kg^{-1} (c) Daily average of the thermocline depth at $DML_{shallow}$ (same data as the solid red line in Fig. 4c), together with the mean depths of $M1_{lower}$ and $M3_{lower}$.

5 Discussion

Our findings - the seasonal spreading of ASW offshore and the role of freshwater input - help to refine the seasonality of the baroclinic component of the ASF/ASC, complementing previous findings. Based on our observations, we summarize the seasonality in three phases (Fig. 10):

In November (Fig. 10a), the ASF is weak (Fig. 10e), as the thermocline is shoaling at DML_{shallow} and deepening at DML_{deep} . At the same time, the absence of ASW results in a weak meridional density gradient at all depths and thus a baroclinic velocity minimum (Fig. 10f and Fig. 5a). Sea ice melt from September and on provides freshwater to the upper ocean and leads to the formation of ASW (Fig. 10d). The regional ocean stress is weak (Fig. 10g), resulting in reduced ASF steepening.

In March (Fig. 10b), sea ice concentration and surface salinity are around their seasonal minima (Fig. 10d), and ASW has been accumulated at the coast to form a secondary front, resulting in an increase in upper-ocean baroclinic velocity (Fig. 10f and Fig. 5a). Maximum ocean stress (Fig. 10g) further aids in steepening the isopycnals. Due to the large density difference between ASW and WW, strong eddy overturning may happen at the secondary front.

The secondary front weakens in June (Fig. 10c) since no new ASW is formed after March. The remainder of the ASW spreads and deepens offshore, possibly via eddy overturning of the secondary front when ocean stress forcing weakens (Fig. 10g). Brine release from sea ice formation (Fig. 10d) along the coast as of March also starts to erode the ASW through convection, as described in section 4.1.1 and corroborated by small vertical salinity gradients between surface and depth between July and November in the H18 data (Fig. 4b). The ASF is around its steepest state, as the thermocline deepens at DML_{shallow} and shoals at DML_{deep} (Fig. 10e). The maximum upper-ocean baroclinic velocity is reached around April (H18) to June (mooring data, Fig. 10f and Fig. 5a). After this phase, weak ocean stress and further brine release cause a relaxation of the ASF and form the transition back to the first phase (Fig. 10a).

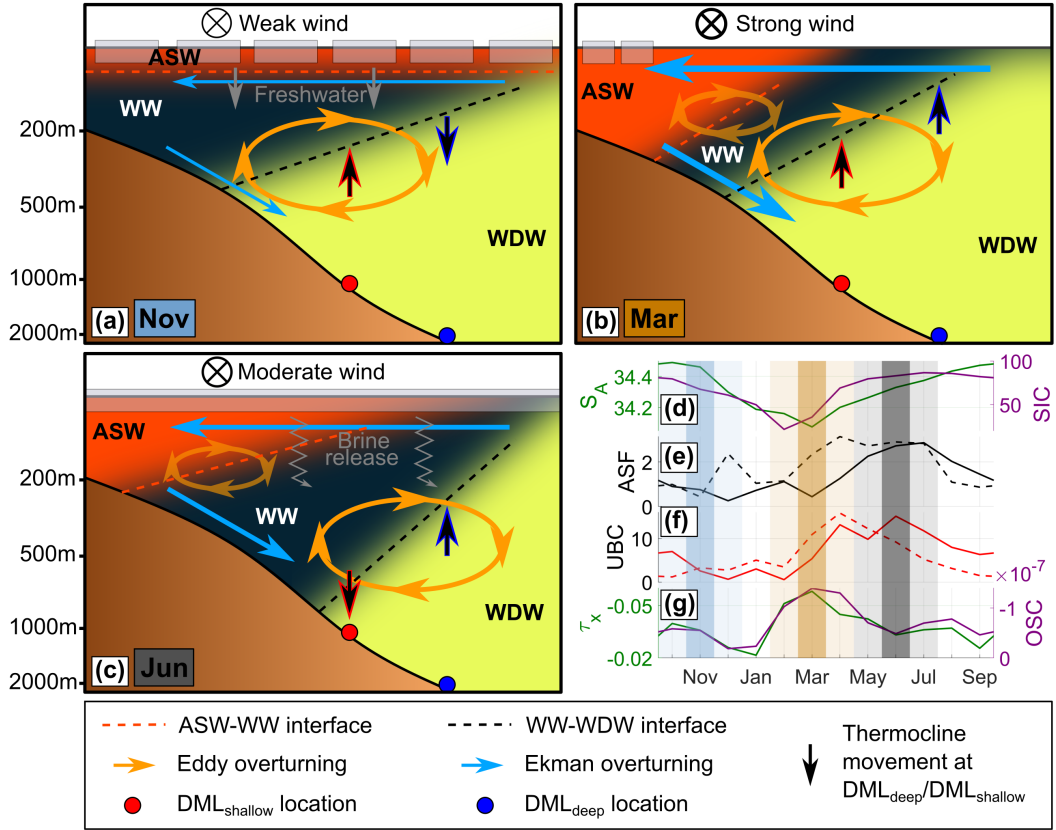


Figure 10. Sketches of different phases of the baroclinic seasonal cycle during (a) November, (b) March, and (c) June. Seasonal time series of relevant variables, i.e. (d) surface absolute salinity over DML_{shallow} isobath from H18 data and sea ice concentration climatology (2010-2021) at DML_{shallow}, (e) mean seasonal ASF slope between DML_{deep} and DML_{shallow} from mooring observations and H18 data, (f) mean seasonal mooring and H18 baroclinic velocity at DML_{shallow} at 100 m depth, and (g) zonal ocean stress (left axis) and ocean stress curl (right axis) climatology (2010-2021) averaged over 0–15°E and 69.5–70°S/67–69.5°S, respectively. Colored shadings indicate the timing of the sketches in panels a-c.

521 We find the barotropic component of the ASC at 6°E to be forced by upstream ocean
 522 stress, consistent with results from earlier studies (Núñez-Riboni & Fahrbach, 2009; Gra-
 523 ham et al., 2013; Le Paih et al., 2020). However, in contrast to Núñez-Riboni and Fahrbach
 524 (2009) at the prime meridian, we do not find a conclusive offshore lag in the seasonal-
 525 ity of the barotropic component in the mooring records or H18 data. Instead, we observe
 526 a clear offshore lag in subsurface salinity, thermocline depth, and resulting surface baro-
 527 clinic velocity seasonality in both data sets. Interestingly, the moorings from Núñez-Riboni

528 and Fahrbach (2009) show a delay of one to three months in long-term temperature sea-
 529 sonality at 200 m and 700 m depth over the 3500 m isobath compared to the 2000 m iso-
 530 bath (Fig. S4 in Supporting Information S1 and Fig. 5 in Le Paih et al., 2020). This is
 531 in agreement with our observed temperature seasonalities at the DML moorings and there-
 532 fore consistent with the offshore lag in thermocline depth seasonality at 6°E and 17°W.
 533 In fact, Núñez-Riboni and Fahrbach (2009) assumed the depth-weighted average of the
 534 total observed velocity to be the barotropic component, to which the observed offshore
 535 delay in ASC strength was attributed. With this approach, however, the barotropic ve-
 536 locity may still contain a significant baroclinic component. Our study shows that the largest
 537 offshore delay occurs in the baroclinic component and not, or at least to a lesser extent,
 538 in the barotropic component. We therefore suggest that sea ice causes the observed off-
 539 shore delay in the ASC seasonality mainly in the baroclinic component through seasonal
 540 meltwater input and offshore spreading.

541 There is an apparent link between seasonal variations in both the baroclinic and
 542 barotropic ASC strength and flow into the Fimbulisen cavity. While not investigated here
 543 in detail, this link may include an intricate interplay between the local bathymetry at
 544 the sills (Nøst, 2004; Eisermann et al., 2020), a seasonal counter-current at depth (Heywood
 545 et al., 1998; Smedsrud et al., 2006; Núñez-Riboni & Fahrbach, 2009; Chavanne et al., 2010),
 546 bottom Ekman transport anomalies (Smedsrud et al., 2006; Núñez-Riboni & Fahrbach,
 547 2009) and potential vorticity constraints (Daae et al., 2017; Wåhlin et al., 2020; Steiger
 548 et al., 2022). The absence of a clear relation between the observed offshore thermocline
 549 depth and the inflow temperature is surprising and points to that warm inflows are rather
 550 controlled by local sub-monthly variations in thermocline depth, forced by variability in
 551 winds, sea ice and SSH (Lauber, Hattermann, et al., 2023). In addition, the internal cav-
 552 ity circulation likely also affects the hydrography at the sill, and the seasonal oceanic vari-
 553 ability below Fimbulisen will be investigated in more detail in a follow-up study.

554 **6 Summary and Conclusions**

555 Our combined analyses of new mooring observations, climatological hydrography,
 556 and satellite-derived surface geostrophic currents have shown that the cross-slope pro-
 557 cesses controlling the ASF/ASC seasonality are consistent along the DML coast across
 558 independent data sets over multiple years in isobath-depth space: in the mooring data
 559 at 6°E, we found the seasonal upper-ocean salinity minimum and thermocline depth max-

imum to occur up to six months later over 2200 m isobath than over 1100 m isobath. The same feature occurs in climatological hydrography at 17°W and translates onto satellite-derived surface geostrophic currents. Our analyses suggest that this offshore delay originates from a seasonal offshore spreading of ASW through eddy overturning at the ASF and the secondary front above. We found the seasonal production of ASW via sea ice melt and subsequent shoreward accumulation to govern the timing of the baroclinic ASC maximum, while variations in ocean stress forcing can additionally modulate the baroclinic seasonality. These findings led us to define three distinct phases describing the seasonality of the ASF/ASC (Fig. 10). These phases may be regarded as generally valid in the Fresh Shelf regime along the East Antarctic coast. Below Fimbulisen, seasonal flow into and out of the cavity is associated with seasonal variations in ASC strength, but the inflow temperature does not follow the offshore thermocline depth. The results of this study contribute to a better understanding of the seasonal variability of the ASF/ASC system along the DML coast and will aid in assessing the impacts of a changing climate on the ASF/ASC.

Data Availability Statement

The DML mooring data will be made available via <https://data.npolar.no> during the revisions. The sub-ice-shelf mooring data will be updated at <https://doi.org/10.21334/npolar.2023.4a6c36f5> (Lauber, de Steur, et al., 2023). The H18 climatology is available at <https://doi.org/10.1594/PANGAEA.893199> (Hattermann & Rohardt, 2018). Sea surface height is available at <https://doi.org/10.17882/81032> (Auger et al., 2021). Sea ice concentration is available at <https://doi.org/10.5067/MPYG15WAA4WX> (DiGirolamo et al., 2022) and sea ice velocity at <https://doi.org/10.5067/INAWUW07QH7B> (Tschudi et al., 2019). ERA5 wind data are available at <https://doi.org/10.24381/cds.f17050d7> (Hersbach et al., 2023). Bathymetric data are available at <https://doi.org/10.1594/PANGAEA.937574> (Dorschel et al., 2022).

Acknowledgments

This research was funded by the Research Council of Norway through the KLIMAFORSK program (iMelt, 295075). The DML moorings were financed and installed by the Norwegian Polar Institute. The installation of the M1 and M3 moorings through the project "ICE Fimbulisen – top to bottom" was financed by the Centre for Ice, Climate and Ecosys-

591 tems (ICE), Norwegian Polar Institute (NPI). The latter moorings were maintained by
 592 NPI through ICE, the Norwegian Antarctic Research Expedition (IceRises 759, 3801-
 593 103), and iMelt. J.L. was funded by iMelt, and T.H. by the European Union’s Horizon
 594 2020 programme (CRiceS, 101003826). We thank the sections Maritime and Technical
 595 Support and Operations and Logistics Antarctica from NPI for all their support involv-
 596 ing the moorings.

597 References

- 598 Armitage, T. W. K., Kwok, R., Thompson, A. F., & Cunningham, G. (2018).
 599 Dynamic Topography and Sea Level Anomalies of the Southern Ocean: Vari-
 600 ability and Teleconnections. *Journal of Geophysical Research: Oceans*, *123*,
 601 613-630.
- 602 Auger, M., Prandi, P., & Sallée, J.-B. (2022). Southern ocean sea level anomaly
 603 in the sea ice-covered sector from multimission satellite observations. *Scientific*
 604 *Data*, *9*(70), 1-10.
- 605 Auger, M., Prandi, P., & Sallée, J.-B. (2021). Daily Southern Ocean Sea Level
 606 Anomaly And Geostrophic Currents from multimission altimetry, 2013-
 607 2019. *SEANOE*. (URL: <https://doi.org/10.17882/81032>. Last accessed:
 608 13.06.2022)
- 609 Auger, M., Sallée, J.-B., Prandi, P., & Naveira Garabato, A. C. (2022). Subpo-
 610 lar Southern Ocean Seasonal Variability of the Geostrophic Circulation From
 611 Multi-Mission Satellite Altimetry. *Journal of Geophysical Research: Oceans*,
 612 *127*, 1-16.
- 613 Chavanne, C. P., Heywood, K. J., Nicholls, K. W., & Fer, I. (2010). Observa-
 614 tions of the Antarctic Slope Undercurrent in the southeastern Weddell Sea.
 615 *Geophysical Research Letters*, *37*(L13601), 1-5. Retrieved from [https://](https://agupubs.onlinelibrary.wiley.com/doi/abs/10.1029/2010GL043603)
 616 agupubs.onlinelibrary.wiley.com/doi/abs/10.1029/2010GL043603 doi:
 617 <https://doi.org/10.1029/2010GL043603>
- 618 Daae, K., Hattermann, T., Darelius, E., & Fer, I. (2017). On the effect of to-
 619 pography and wind on warm water inflow — An idealized study of the
 620 southern Weddell Sea continental shelf system. *Journal of Geophys-*
 621 *ical Research: Oceans*, *122*(3), 2622-2641. Retrieved from [https://](https://agupubs.onlinelibrary.wiley.com/doi/abs/10.1002/2016JC012541)
 622 agupubs.onlinelibrary.wiley.com/doi/abs/10.1002/2016JC012541 doi:

- 623 <https://doi.org/10.1002/2016JC012541>
- 624 Deacon, G. (1979). The Weddell gyre. *Deep Sea Research Part A. Oceanographic*
 625 *Research Papers*, 26(9), 981-995. Retrieved from [https://www.sciencedirect](https://www.sciencedirect.com/science/article/pii/019801497990044X)
 626 [.com/science/article/pii/019801497990044X](https://www.sciencedirect.com/science/article/pii/019801497990044X) doi: 10.1016/0198-0149(79)
 627 90044-X
- 628 DiGirolamo, N., Parkinson, C. L., Cavalieri, D. J., Gloersen, P., & Zwally, H. J.
 629 (2022). Sea Ice Concentrations from Nimbus-7 SMMR and DMSP SSM/I-
 630 SSMIS Passive Microwave Data, Version 2. [March 2019 to January 2021,
 631 180°W - 180°E and 90°S - 40°S]. *NASA National Snow and Ice Data Cen-*
 632 *ter Distributed Active Archive Center. Boulder/Colorado/USA..* (URL:
 633 <https://doi.org/10.5067/MPYG15WAA4WX>. Last accessed: 21.11.2022)
- 634 Dorschel, B., Hehemann, L., Viquerat, S., Warnke, F., Dreutter, S., Schulze
 635 Tenberge, Y., ... Arndt, J. E. (2022). The International Bathymetric
 636 Chart of the Southern Ocean Version 2 (IBCSO v2). *PANGAEA.* (URL:
 637 <https://doi.org/10.1594/PANGAEA.937574>. Last accessed: 15.06.2022)
- 638 Dorschel, B., Hehemann, L., Viquerat, S., Warnke, F., Dreutter, S., Tenberge, Y. S.,
 639 ... others (2022). The International Bathymetric Chart of the Southern Ocean
 640 Version 2. *Scientific Data*, 9(275), 1-13.
- 641 Dotto, T. S., Naveira Garabato, A., Bacon, S., Tsamados, M., Holland, P. R., Hoo-
 642 ley, J., ... Meredith, M. P. (2018). Variability of the Ross Gyre, Southern
 643 Ocean: Drivers and Responses Revealed by Satellite Altimetry. *Geophysical*
 644 *Research Letters*, 45, 6195-6204.
- 645 Eisermann, H., Eagles, G., Ruppel, A., Smith, E. C., & Jokat, W. (2020).
 646 Bathymetry Beneath Ice Shelves of Western Dronning Maud Land, East
 647 Antarctica, and Implications on Ice Shelf Stability. *Geophysical Research*
 648 *Letters*, 47(12), 1-10.
- 649 Gordon, A., Martinson, D., & Taylor, H. (1981). The wind-driven circula-
 650 tion in the Weddell-Enderby Basin. *Deep Sea Research Part A. Oceanographic*
 651 *Research Papers*, 28(2), 151-163. Retrieved from [https://](https://www.sciencedirect.com/science/article/pii/019801498190087X)
 652 www.sciencedirect.com/science/article/pii/019801498190087X doi:
 653 10.1016/0198-0149(81)90087-X
- 654 Graham, J. A., Heywood, K. J., Chavanne, C. P., & Holland, P. R. (2013). Seasonal
 655 variability of water masses and transport on the Antarctic continental shelf

- 656 and slope in the southeastern Weddell Sea. *Journal of Geophysical Research:*
 657 *Oceans*, 118(4), 2201-2214.
- 658 Haran, T., Klinger, M., Bohlander, J., Fahnestock, M., Painter, T., & Scambos,
 659 T. (2018). MEaSURES MODIS Mosaic of Antarctica 2013-2014 (MOA2014)
 660 Image Map, Version 1. [moa750_2014.hp1_v01.tif]. *NASA National Snow and*
 661 *Ice Data Center Distributed Active Archive Center. Boulder/Colorado/USA..*
 662 (URL: <https://nsidc.org/data/NSIDC-0730/versions/1>. Last accessed:
 663 25.08.2021)
- 664 Hattermann, T. (2018). Antarctic Thermocline Dynamics along a Narrow Shelf with
 665 Easterly Winds. *Journal of Physical Oceanography*, 48(10), 2419-2443.
- 666 Hattermann, T., Nøst, O. A., Lilly, J. M., & Smedsrud, L. H. (2012). Two years of
 667 oceanic observations below the Fimbul Ice Shelf, Antarctica. *Geophysical Re-*
 668 *search Letters*, 39(12), 1-6.
- 669 Hattermann, T., & Rohardt, G. (2018). Kapp Norvegia Antarctic Slope Front clima-
 670 tology. *Alfred Wegener Institute, Helmholtz Centre for Polar and Marine Re-*
 671 *search, Bremerhaven, PANGAEA.* (URL: [https://doi.org/10.1594/PANGAEA](https://doi.org/10.1594/PANGAEA.893199)
 672 [.893199](https://doi.org/10.1594/PANGAEA.893199). Last accessed: 24.08.2022)
- 673 Hersbach, H., Bell, B., Berrisford, P., Biavati, G., Horányi, A., Muñoz Sabater, J.,
 674 ... Thépaut, J.-N. (2023). ERA5 monthly averaged data on single levels from
 675 1940 to present. *Copernicus Climate Change Service (C3S) Climate Data Store*
 676 *(CDS).* (URL: <https://doi.org/10.24381/cds.f17050d7>. Last accessed:
 677 02.11.2021)
- 678 Heywood, K. J., Locarnini, R. A., Frew, R. D., Dennis, P. F., & King, B. A. (1998).
 679 Transport and Water Masses of the Antarctic Slope Front System in The
 680 Eastern Weddell Sea. In S. S. Jacobs & R. F. Weiss (Eds.). *Ocean, ice, and*
 681 *atmosphere: Interactions at the Antarctic continental margin, Antarctic Re-*
 682 *search Series.*, 75, 203-214. Retrieved from [https://agupubs.onlinelibrary](https://agupubs.onlinelibrary.wiley.com/doi/abs/10.1029/AR075p0203)
 683 [.wiley.com/doi/abs/10.1029/AR075p0203](https://agupubs.onlinelibrary.wiley.com/doi/abs/10.1029/AR075p0203) (Washington, DC: American
 684 Geophysical Union) doi: <https://doi.org/10.1029/AR075p0203>
- 685 Huneke, W. G. C., Morrison, A. K., & Hogg, A. M. (2022). Spatial and Suban-
 686 nual Variability of the Antarctic Slope Current in an Eddyding Ocean–Sea
 687 Ice Model. *Journal of Physical Oceanography*, 52(3), 347 - 361. Re-
 688 trieved from <https://journals.ametsoc.org/view/journals/phoc/52/>

- 689 3/JPO-D-21-0143.1.xml doi: <https://doi.org/10.1175/JPO-D-21-0143.1>
- 690 Isachsen, P. E., LaCasce, J. H., Mauritzen, C., & Häkkinen, S. (2003). Wind-
 691 Driven Variability of the Large-Scale Recirculating Flow in the Nordic
 692 Seas and Arctic Ocean. *Journal of Physical Oceanography*, 33(12), 2534 -
 693 2550. Retrieved from [https://journals.ametsoc.org/view/journals/
 694 phoc/33/12/1520-0485_2003_033_2534_wvotlr_2.0.co_2.xml](https://journals.ametsoc.org/view/journals/phoc/33/12/1520-0485_2003_033_2534_wvotlr_2.0.co_2.xml) doi:
 695 10.1175/1520-0485(2003)033<2534:WVOTLR>2.0.CO;2
- 696 Jacobs, S. S. (1991). On the nature and significance of the Antarctic Slope Front.
 697 *Marine Chemistry*, 35(1), 9-24. doi: [https://doi.org/10.1016/S0304-4203\(09\)
 698 90005-6](https://doi.org/10.1016/S0304-4203(09)90005-6)
- 699 Lauber, J., de Steur, L., Hattermann, T., & Nøst, O. A. (2023). Daily averages of
 700 physical oceanography and current meter data from sub-ice-shelf moorings M1,
 701 M2 and M3 at Fimbulisen, East Antarctica since 2009. *Norwegian Polar In-
 702 stitute, Tromsø*. (URL: <https://doi.org/10.21334/npolar.2023.4a6c36f5>.
 703 Last accessed: 07.07.2023)
- 704 Lauber, J., Hattermann, T., de Steur, L., Darelius, E., Auger, M., Nøst, O., &
 705 Moholdt, G. (2023). Warming beneath an East Antarctic ice shelf due to
 706 increased subpolar westerlies and reduced sea ice. *Nature Geoscience*. doi:
 707 10.1038/s41561-023-01273-5
- 708 Le Paih, N., Hattermann, T., Boebel, O., Kanzow, T., Lüpkes, C., Rohardt, G.,
 709 ... Herbette, S. (2020). Coherent Seasonal Acceleration of the Weddell Sea
 710 Boundary Current System Driven by Upstream Winds. *Journal of Geophysical
 711 Research: Oceans*, 125(e2020JC016316), 1-20.
- 712 Martin, T., Tsamados, M., Schroeder, D., & Feltham, D. L. (2016). The impact of
 713 variable sea ice roughness on changes in Arctic Ocean surface stress: A model
 714 study. *Journal of Geophysical Research: Oceans*, 121, 1931-1952.
- 715 Mathiot, P., Goosse, H., Fichefet, T., Barnier, B., & Gallée, H. (2011). Modelling
 716 the seasonal variability of the Antarctic Slope Current. *Ocean Science*, 7, 455-
 717 470. doi: <https://doi.org/10.5194/os-7-455-2011>
- 718 McDougall, T. J., & Barker, P. M. (2011). Getting started with TEOS-10 and the
 719 Gibbs Seawater (GSW) Oceanographic Toolbox. *Scor/Iapso WG127*, 1-32.
- 720 Nakayama, Y., Greene, C. A., Paolo, F. S., Mensah, V., Zhang, H., Kashiwase, H.,
 721 ... Aoki, S. (2021). Antarctic Slope Current Modulates Ocean Heat Intrusions

- 722 Towards Totten Glacier. *Geophysical Research Letters*, *48*(17), 1-10.
- 723 Naveira Garabato, A. C., Dotto, T. S., Hooley, J., Bacon, S., Tsamados, M., Ridout,
724 A., ... Meredith, M. P. (2019). Phased Response of the Subpolar South-
725 ern Ocean to Changes in Circumpolar Winds. *Geophysical Research Letters*,
726 *46*(11), 6024-6033.
- 727 Neme, J., England, M. H., & Hogg, A. M. (2021). Seasonal and Interannual Vari-
728 ability of the Weddell Gyre From a High-Resolution Global Ocean-Sea Ice
729 Simulation During 1958–2018. *Journal of Geophysical Research: Oceans*, *126*,
730 1-19.
- 731 Nøst, O. A. (2004). Measurements of ice thickness and seabed topography under
732 the Fimbul Ice Shelf, Dronning Maud Land, Antarctica. *Journal of Geophysi-
733 cal Research: Oceans*, *109*, 1-14.
- 734 Nøst, O. A., Biuw, M., Tverberg, V., Lydersen, C., Hattermann, T., Zhou, Q., ...
735 Kovacs, K. M. (2011). Eddy overturning of the Antarctic Slope Front controls
736 glacial melting in the Eastern Weddell Sea. *Journal of Geophysical Research:
737 Oceans*, *116*, 1-17.
- 738 Núñez-Riboni, I., & Fahrbach, E. (2009). Seasonal variability of the Antarctic
739 Coastal Current and its driving mechanisms in the Weddell Sea. *Deep Sea
740 Research Part I: Oceanographic Research Papers*, *56*(11), 1927-1941.
- 741 Pauthenet, E., Sallée, J.-B., Schmidtko, S., & Nerini, D. (2021). Seasonal Varia-
742 tion of the Antarctic Slope Front Occurrence and Position Estimated from an
743 Interpolated Hydrographic Climatology. *Journal of Physical Oceanography*,
744 *51*(5), 1539 - 1557. Retrieved from [https://journals.ametsoc.org/view/
745 journals/phoc/51/5/JPO-D-20-0186.1.xml](https://journals.ametsoc.org/view/journals/phoc/51/5/JPO-D-20-0186.1.xml) doi: [https://doi.org/10.1175/
746 JPO-D-20-0186.1](https://doi.org/10.1175/JPO-D-20-0186.1)
- 747 Si, Y., Stewart, A. L., & Eisenman, I. (2023). Heat transport across the Antarc-
748 tic Slope Front controlled by cross-slope salinity gradients. *Science Advances*,
749 *9*(18), 1-12. Retrieved from [https://www.science.org/doi/abs/10.1126/
750 sciadv.add7049](https://www.science.org/doi/abs/10.1126/sciadv.add7049) doi: 10.1126/sciadv.add7049
- 751 Smedsrud, L. H., Jenkins, A., Holland, D. M., & Nøst, O. A. (2006). Modeling
752 ocean processes below Fimbulisen, Antarctica. *Journal of Geophysical Re-
753 search: Oceans*, *111*, 1-13.
- 754 Steiger, N., Darelius, E., Kimura, S., Patmore, R. D., & Wählin, A. K. (2022).

- 755 The Dynamics of a Barotropic Current Impinging on an Ice Front. *Journal*
 756 *of Physical Oceanography*, 52(12), 2957 - 2973. Retrieved from [https://](https://journals.ametsoc.org/view/journals/phoc/52/12/JPO-D-21-0312.1.xml)
 757 journals.ametsoc.org/view/journals/phoc/52/12/JPO-D-21-0312.1.xml
 758 doi: 10.1175/JPO-D-21-0312.1
- 759 Stewart, A. L., Klocker, A., & Menemenlis, D. (2019). Acceleration and Over-
 760 turning of the Antarctic Slope Current by Winds, Eddies, and Tides. *Journal*
 761 *of Physical Oceanography*, 49(8), 2043 - 2074. Retrieved from [https://](https://journals.ametsoc.org/view/journals/phoc/49/8/jpo-d-18-0221.1.xml)
 762 journals.ametsoc.org/view/journals/phoc/49/8/jpo-d-18-0221.1.xml
 763 doi: 10.1175/JPO-D-18-0221.1
- 764 Stewart, A. L., & Thompson, A. F. (2015). Eddy-mediated transport of warm Cir-
 765 cumpolar Deep Water across the Antarctic Shelf Break. *Geophysical Research*
 766 *Letters*, 42(2), 432-440. Retrieved from [https://agupubs.onlinelibrary](https://agupubs.onlinelibrary.wiley.com/doi/abs/10.1002/2014GL062281)
 767 [.wiley.com/doi/abs/10.1002/2014GL062281](https://agupubs.onlinelibrary.wiley.com/doi/abs/10.1002/2014GL062281) doi: 10.1002/2014GL062281
- 768 Sverdrup, H. U. (1954). The Currents off the Coast of Queen Maud Land. *Norsk*
 769 *Geografisk Tidsskrift*, 14(1-4), 239-249.
- 770 Thompson, A. F., Heywood, K. J., Schmidtko, S., & Stewart, A. L. (2014). Eddy
 771 transport as a key component of the Antarctic overturning circulation. *Nature*
 772 *Geosciences*, 7, 879-884.
- 773 Thompson, A. F., Stewart, A. L., Spence, P., & Heywood, K. J. (2018). The Antarc-
 774 tic Slope Current in a Changing Climate. *Reviews of Geophysics*, 56, 741-770.
- 775 Tsamados, M., Feltham, D. L., Schroeder, D., Flocco, D., Farrell, S. L., Kurtz, N.,
 776 ... Bacon, S. (2014). Impact of Variable Atmospheric and Oceanic Form Drag
 777 on Simulations of Arctic Sea Ice. *Journal of Physical Oceanography*, 44(5),
 778 1329 - 1353.
- 779 Tschudi, M., Meier, W. N., Stewart, J. S., Fowler, C., & Maslanik, J. (2019). Po-
 780 lar Pathfinder Daily 25 km EASE-Grid Sea Ice Motion Vectors, Version 4.
 781 [March 2019 to January 2021, 180°W - 180°E and 90°S - 37°S]. *NASA Na-*
 782 *tional Snow and Ice Data Center Distributed Active Archive Center. Boul-*
 783 *der/Colorado/USA..* (URL: <https://doi.org/10.5067/INAWUW07QH7B>. Last
 784 accessed: 08.03.2022)
- 785 Vernet, M., Geibert, W., Hoppema, M., Brown, P. J., Haas, C., Hellmer, H. H., ...
 786 Verdy, A. (2019). The Weddell Gyre, Southern Ocean: Present Knowledge
 787 and Future Challenges. *Reviews of Geophysics*, 57(3), 623-708. Retrieved

788 from <https://agupubs.onlinelibrary.wiley.com/doi/abs/10.1029/>

789 2018RG000604 doi: 10.1029/2018RG000604

790 Wåhlin, A. K., Steiger, N., Darelius, E., Assmann, K. M., Glessmer, M. S., Ha,

791 H. K., ... Viboud, S. (2020). Ice front blocking of ocean heat transport to an

792 Antarctic ice shelf. *Nature*, 578(7796), 568-571.

793 Webb, D. J., Holmes, R. M., Spence, P., & England, M. H. (2022). Propagation of

794 barotropic Kelvin waves around Antarctica. *Ocean Dynamics*, 72, 405-419.

795 Zhou, Q., Hattermann, T., Nøst, O. A., Biuw, M., Kovacs, K. M., & Lydersen, C.

796 (2014). Wind-driven spreading of fresh surface water beneath ice shelves in

797 the Eastern Weddell Sea. *Journal of Geophysical Research: Oceans*, 119,

798 3818-3833.